Accepted Manuscript

Multidimensional extension of the continuity equation method for debris clouds evolution

Francesca Letizia, Camilla Colombo, Hugh G. Lewis
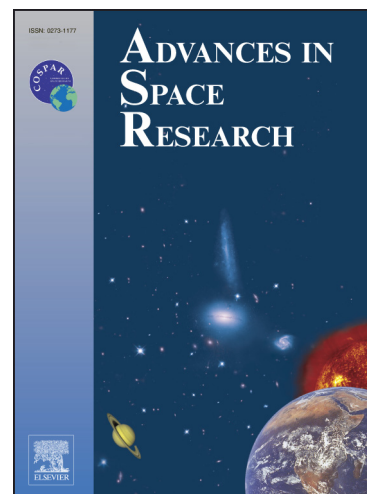
Multidimensional extension of the continuity equation method for debris clouds evolution

Francesca Letizia[*]

Astronautics Research Group, University of Southampton, Southampton, UK

Camilla Colombo

Department of Aerospace Science and Technology, Politecnico di Milano, Milano, Italy

Hugh G. Lewis

Astronautics Research Group, University of Southampton, Southampton, UK

Abstract

As the debris spatial density increases due to recent collisions and inoperative spacecraft, the probability of collisions in space grows. Even a collision involving small objects may produce thousands of fragments due to the high orbital velocity and the high energy released. The propagation of the trajectories of all the objects produced by a breakup would be prohibitive in terms of computational time; therefore, simplified models are needed to describe the consequences of a collision with a reasonable computational effort. The continuity approach can be applied to this purpose as it allows switching the point of view from the analysis of each single fragment to the study of the evolution of the debris cloud globally. Previous formulations of the continuity equation approach focussed on the representation of the drag effect on the fragment spatial density. This work proposes how the continuity equation approach can be extended to multiple dimensions in the phase space defined by the relevant orbital parameters. This novel approach allows including in the propagation also the effect of the Earth's oblateness and improving the description of the drag effect by considering the

---

[*]Corresponding author
 Email address: `f.letizia@soton.ac.uk` (Francesca Letizia)

distribution of area-to-mass ratio and eccentricity among the fragments. Results for these three applications are shown and discussed in terms of accuracy compared to the numerical propagation and to the one-dimensional approach.

Keywords: space debris, continuity equation, debris cloud, fragments propagation

1. Introduction

More than 17000 objects larger than 5 cm are in orbit around the Earth and are constantly tracked from the Earth to avoid collisions for operational satellites (IADC Steering Committee, 2013)[1]. The population of centimetre-sized objects can be statistically derived from radar data and the number of even smaller objects is inferred from impact records (Xu et al., 2009). Even if these small objects are not catalogued individually, they can still be dangerous. Any object larger than 1 cm is supposed to be able to destroy a satellite in case of collision (McKnight et al., 2014) and objects as small as 1 mm can cause relevant anomalies on spacecraft operations, leading sometime to the failure of the mission. In addition, small fragments are usually not included in studies on the long term evolution of debris population because their number is so large (i.e., more than several hundred of thousands objects larger than 1 cm) that the computational time would be prohibitive. On the other hand, excluding small objects from these analyses may result in underestimating the collision risk or in misinterpreting the effect of mitigation and remediation measures (White and Lewis, 2014).

Including small fragments in debris models demands the development of simplified approaches to describe fragment cloud evolution in a reasonable computational time. Analytical models can be used to this purpose; they have been proposed mainly for short term analysis (Hoots and Hansen, 2014) or for the Geosynchronous Earth Orbit (GEO) region (Valk et al., 2009; Izzo, 2002), where

---

[1]The catalogued objects can be checked at https://www.space-track.org: currently, 17141 objects are present in the catalogue, out of which 4054 are active.

the forces admit a Hamiltonian representation. Only one fully analytical model, proposed by McInnes (1993), appears to be applicable to Low Earth Orbits (LEO), where the debris density is the highest. The main idea of this approach is to consider the debris population as a fluid with continuous properties, whose density changes under the effect of drag and collisions. In this way, the analysis of the single object is abandoned and the fragment density is used as the only parameter of interest.

The evolution of the density is obtained through the continuity equation, a traditional approach in fluid-dynamics, where it is used to link the fluid density with its velocity. Similarly, when applied in astrodynamics, it allows describing the change in the density of a dispersed set starting from the knowledge of the velocities of the particles. In particular, if n represents the fragment density, the continuity equation can be written as

$$\frac{\partial n}{\partial t} + \nabla \cdot \mathbf{f} = \dot{n}^+ - \dot{n}^- \tag{1}$$

where $\nabla \cdot \mathbf{f}$ models the forces acting on the system and accounts for *slow*/ continuous phenomena (such as perturbations) and $\dot{n}^+ - \dot{n}^-$ represents the sources and the sinks of the system, so it can models *fast*/discontinuous events (e.g., the injection of new fragments due to launches). Once the initial distribution of n is known, the continuity equation is used to obtain its evolution with time, with very low computational effort.

The method is general and it has been applied also to describe the evolution of interplanetary dust (Gor'kavyi, 1997; Gor'kavyi et al., 1997), nano-satellites constellations (McInnes, 2000) and high area-to-mass spacecraft (Colombo and McInnes, 2011). In all these cases, continuous and/or discontinuous phenomena have to be described, as summarised in Table 1.

One can observe from Table 1 that the continuity equation can be used to find the evolution of the system both in the physical space (such as in the examples on space debris and nanosatellites, where the variables of the problem are time and distance from Earth) and in the phase space (such as in the examples on

3

interplanetary dust and high area-to-mass ratio objects, where orbital elements are used to represent the solution space). This makes the method very flexible as it is possible to describe the evolution of the studied system in the relevant space with the simplest formulation.

The formulation with the continuity equation is comparable to the one by Nazarenko (1997) and Smirnov et al. (2001), who describe the evolution of the debris population through the equation

$$\frac{\partial N_j}{\partial t} = -W_j \frac{\partial N_j}{\partial r} - N_j \frac{\partial W_j}{\partial r} + \dot{N}_j \qquad (2)$$

where $N_j(r,t)$ is the number of debris objects in the jth bin in terms of size, perigee altitude, eccentricity, inclination, ballistic coefficient. W_j is the radial velocity of the objects and $\dot{N}_j$ is the rate of variation in the number of objects due to external causes. It is easy to recognise the connection between Equation 2 and Equation 1, considering that the second and the third term in Equation 2 can be obtained from Equation 1 considering the dependence on the radial distance only and writing the divergence in cartesian coordinates. Nazarenko (2002) discussed the advantages of adopting a statistical model based on density for space debris propagation compared to deterministic models. These include a reduction in the computational time, the possibility of including objects of any size and a more natural connection to the statistical nature of the problem (i.e. fragment distribution with uncertain initial conditions).

The approach presented in this work aims to exploit these advantages for

Table 1: Summary of the applications of the continuity equation method to astrodynamics. a and e are the orbit semi-major axis and eccentricity; r is the distance from the central body; t is the time; Φ the angle between the Sun-Earth line and the direction of the orbit pericentre.

Application	Solution space	Slow phenomena	Fast events	Ref.
Interplanetary dust	(a, e)	Poynting-Robertson drag Planetary resonances	Gravitational scattering Mutual collisions	(Gor'kavyi, 1997) (Gor'kavyi et al., 1997)
Space debris	(r, t)	Atmospheric drag	Mutual collisions Launches	(McInnes, 1993) (Letizia et al., 2015a)
Nanosatellites	(r, t)	Atmospheric drag	Launches and failures	(McInnes, 2000)
High area-to-mass objects	(e, Φ)	Earth's oblateness Solar radiation pressure	-	(Colombo and McInnes, 2011)

the propagation of single debris clouds, instead of the global debris population. Moreover, the formulation in Equation 1 allows further enhancing the convenience of the approach by providing an analytical solution to the problem of debris cloud evolution.

In particular, the case of debris clouds in Low Earth Orbit (LEO) is studied. The evolution of a debris cloud under the effect of perturbations can be studied with a *phased approach*, which splits the evolution into three main phases (Figure 1), each one with different geometry and different driving forces (Jehn, 1991; McKnight, 1990).

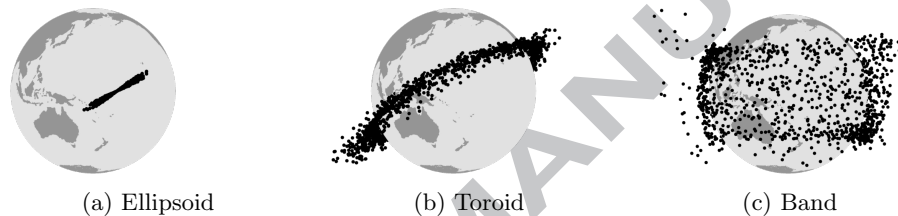(a) Ellipsoid   (b) Toroid   (c) Band

Figure 1: Phases of debris cloud evolution as classified by McKnight (1990) and Jehn (1991). The simulation refers to a collision on a parent orbit with inclination equal to 30°.

In the first phase, the evolution of the cloud is driven by the different energy among the fragments. This causes the cloud to be stretched along the parent orbit, so that the mean anomaly M is randomised within a few orbits. In this phase, the dynamics of the system is usually studied applying the two-body problem equations.

In the following phases, the effect of perturbations drives the cloud evolution. The Earth's oblateness causes the nodal precession of the orbits, resulting into the spreading of the argument of the periapsis ω and of the longitude of the ascending node Ω. This transforms the cloud into a band around the Earth, limited in latitude by the value of inclination of the parent orbit (Figure 1c).

Once the band has formed, ω and Ω can be considered uniformly distributed: as a results, the forces acting on ν, ω, Ω, as the Earth's oblateness, are not relevant over the long term (Rossi et al., 1998). In this phase, drag becomes the dominant perturbation and it is possible to apply the expressions found by

5

McInnes (1993) to describe the long term evolution of the fragment density.

In a previous work (Letizia et al., 2015a), this novel approach to debris propagation was validated and applied to study the evolution of debris fragment clouds generated by collisions in LEO. The method, summarised in Section 2, is able to model the evolution of debris clouds including all the small fragments down to 1 mm in size, with a reduced computational effort compared to the propagation of the individual trajectories. This enabled to perform an extended analysis on the contribution of small fragments to the collision probability (Letizia et al., 2015b), proving that the method can be useful to evaluate the hazard posed by small fragments to operational spacecraft.

This article shows how the analytical formulation proposed by McInnes (1993) can be extended to more dimensions to improve the description of the drag effect and to extend the method applicability to other phases of the cloud evolution. In detail, Section 4 discusses the description of the effect of the Earth's oblateness, i.e., the evolution from the ellipsoid to the band (Figure 1). Section 5 and Section 6 focus on possible improvements of the propagation under the drag effect by considering, respectively, the area-to-mass ratio and eccentricity distributions among the fragments.

2. Continuity equation method for fragmentation modelling

The continuity equation can be applied to study a single fragmentation event by using the approach summarised in the block diagram in Figure 2: a brief description of the proposed analytical model for cloud propagation in LEO (CiELO, debris Cloud Evolution in Low Earth Orbits) is presented here, whereas an extensive explanation of each block can be found in Letizia et al. (2015a).
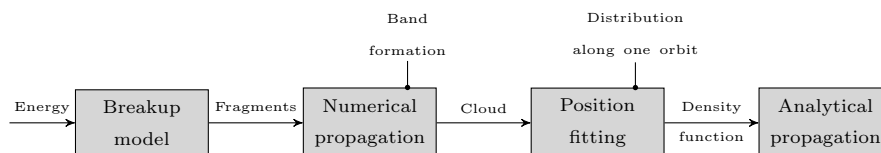
Figure 2: CiELO building blocks.

6

The first block is a *breakup model*, which generates the fragments and their characteristics (e.g., mass, velocity) given the energy of the fragmentation event. The NASA breakup model (Johnson and Krisko, 2001; Krisko, 2011) is used here, considering all fragments between 1 mm and 10 cm. The second block of the method is the *numerical propagation* of the fragment orbital parameters. The numerical propagator used is PlanODyn (Planetary Orbital Dynamics), a semi-analytical method based on averaged Gauss' equations (Colombo, 2015). The numerical method is applied to each fragment to obtain the evolution of its trajectory under the effect of the atmospheric drag and of the Earth's oblateness. For the atmospheric drag, an exponential density model is used; for the Earth's oblateness, only the term J_2 is considered. The numerical method is used in this work for two purposes. Firstly, it is applied to model the phase of the cloud evolution where the Earth's oblateness acts as main perturbation. Secondly, the numerical method is also used to define the baseline against which the results of the analytical method are compared and validated. Future work will validate the analytical model against a more detailed description of the orbital perturbations, in particular including the effect of solar radiation pressure, which is relevant at the altitudes considered in this study.

The time required for the band formation can be estimated starting from the parameters of the initial orbits and the energy of the fragmentation, as done by Ashenberg (1994). Once the band is formed, the third block, *position fitting*, translates the information on each single fragment into a continuous function that describes globally the cloud. The used function is not the simple position distribution of the fragments, but rather it is built from the probability of finding a fragment at a certain geocentric distance given its orbital parameters (semi-major axis a and eccentricity e) (Kessler, 1981; Sykes, 1990). Assuming that all fragments have the same probability and summing all their contribution, the initial density of the cloud (n_0) is defined (Letizia et al., 2015a,b).

Finally, the forth block is the *analytical propagation*, based on the continuity equation (Equation 1), to obtain the long-term evolution of the cloud density. No discontinuous events are considered, so $\dot{n}^+ - \dot{n}^- = 0$; the term $\nabla \cdot \mathbf{f}$ is used to

7

model atmospheric drag, following the approach developed by McInnes (1993, 2000). Assuming the band to be spherically symmetrical, the spatial problem can be studied through only one coordinate, the radial one. In this case, $\mathbf{f}$ has only one component, f_r, that is written as

$$f_r = v_r n(r, t),$$

where v_r is the radial velocity

$$v_r = -\varepsilon \sqrt{r} \exp\left(-\frac{r - R_H}{H}\right). \tag{3}$$

The parameter ε

$$\varepsilon = \sqrt{\mu} \frac{c_D A}{M} \rho_0, \tag{4}$$

collects all the terms that do not depend on r, such as the gravitational constant μ, and the fragment drag coefficient c_D, cross-sectional area A and mass M. R_H, ρ_0, H are, respectively, the fragmentation altitude and the corresponding reference density and scale height deriving from an exponential model for the atmosphere, whose values are here taken from Vallado (2013). The expression for the radial velocity in Equation 4 is rigorously valid only for circular orbits, so this formulation of the problem assumes that all the fragments are on circular orbits. In addition, Equation 3 is further simplified approximating, in the square root, the actual distance of the fragment with the fragmentation distance

$$\sqrt{r} \approx \sqrt{R_H} \tag{5}$$

to obtain a full analytical solution. With these assumptions, the vector field f_r can be written as

$$f_r = -\varepsilon \sqrt{R_H} \exp\left(-\frac{r - R_H}{H}\right) n(r, t); \tag{6}$$

substituting this expression into Equation 1 and writing the divergence in spher-

ical coordinates, the following partial differential equation is obtained

$$\frac{\partial n}{\partial t} + v_r \frac{\partial n}{\partial r} + \left(\frac{2}{r}v_r + \frac{\partial v_r}{\partial r}\right)n(r,t) = 0. \tag{7}$$

Applying the method of characteristics (Evans, 1998), the partial differential equation in Equation 7 can be transformed in the following system of Ordinary Differential Equations (ODE)

$$\begin{cases} \dfrac{dt}{ds} = 1 & (8) \\[2mm] \dfrac{dr}{ds} = v_r(r) & (9) \\[2mm] \dfrac{dn}{ds} = -\left[\dfrac{2}{r}v_r + \dfrac{\partial v_r}{\partial r}\right]n(r,t), & (10) \end{cases}$$

where s expresses a parametrisation of the characteristic lines. From Equations 8 and 9 the expression of the characteristic line is obtained

$$G_r(r,t) = \exp\left(\frac{r - R_H}{H}\right) + \varepsilon \frac{\sqrt{R_H}}{H}t; \tag{11}$$

and from Equations 9 and 10 the explicit expression for the density evolution in time can be written (McInnes, 1993, 2000),

$$n(r,t) = \frac{\Psi\{\exp\left[-\frac{r-R_H}{H}\right] + (\varepsilon\sqrt{R_H}/H)t\}}{-\varepsilon r^{5/2}\exp\left[-\frac{r-R_H}{H}\right]}. \tag{12}$$

The function Ψ is obtained from the initial condition $n(r, t = 0)$ and the expression of the characteristics at the initial time $t = 0$

$$G_r(r,0) = \exp\left(\frac{r - R_H}{H}\right)$$

that is inverted to obtain

$$r_i = R_H + H \log G_r(r,t)$$

9

which finally allows writing an explicit expression for Ψ

$$\Psi(r,t) = n(r_i(r,t),0)r_i(r,t)^2 v_r(r_i(r,t)). \tag{13}$$

This approach provides an accurate description of the evolution of clouds produced by fragmentation events at altitudes higher than 800 km and for any inclination, with a reduced computational effort with respect to of the numerical propagation (Letizia et al., 2015a). Therefore, it can be applied to study many different scenarios of collisions to understand, for example, which objects, in case of fragmentation, are more likely to have a large impact on the global collision risk for operational satellites (Letizia et al., 2015b). This was done by applying the proposed method to compute a grid of fictitious breakups, store the scenario evolution, and evaluate their effect on several targets without having to simulate the fragmentations for each target spacecraft.

However, the one dimensional approach has some limits

- the numerical (semi-analytical) propagation is still required to model the first part of the cloud evolution, where the Earth's oblateness is the main perturbation,

- the fragments in the cloud may have very different values of area-to-mass ratio A/M, a parameter that largely affect their decay in the atmosphere, but this is not captured from the original formulation from McInnes (1993),

- the method can be applied to fragmentation events at 800 km as at lower altitudes the hypothesis of circular orbits in Equation 3 introduces a large error on the evolution of the cloud density (Letizia et al., 2015a).

In this work, we address these three limits of the continuity equation approach by extending it to more than one dimension in the phase space defined by the relevant parameters for the considered problem. Moreover, we derive a general approach to use the continuity equation in any set of phase space variables.

10

3. Formulation of the continuity equation in multiple dimensions

Following the approach by Gor'kavyi et al. (1997), the continuity equation can be written in the phase space by simply writing the divergence in rectangular coordinates. This approach is chosen because the effect of perturbations is usually described in terms of their impact on the orbital parameters (through Gauss' equations). Therefore, the problem is written in the space defined by the relevant orbital parameters to use directly the expression on the orbital parameters variation and to avoid complex transformations to a physical 3D space. If necessary, the results can then be translated into physical coordinates by using expressions such as the already mentioned ones by Kessler (1981) or Sykes (1990) which express the spatial density as a function of the orbital parameters.

Considering m generic variables $(\alpha_1, \ldots, \alpha_m)$ and assuming that n is differentiable with respect to all α everywhere, the Equation 1 can be rewritten using the expression of the divergence in rectangular coordinates

$$\frac{\partial n}{\partial t} + \frac{\partial n}{\partial \alpha_1} v_{\alpha_1} + \cdots + \frac{\partial n}{\partial \alpha_m} v_{\alpha_m} + \left[\frac{\partial v_{\alpha_1}}{\partial \alpha_1} + \cdots + \frac{\partial v_{\alpha_m}}{\partial \alpha_m}\right] n = \dot{n}^+ - \dot{n}^-. \quad (14)$$

The terms of sink and source are neglected also in this case $(\dot{n}^+ - \dot{n}^- = 0)$, so applying the method of characteristics the following system of ODEs is obtained

$$\begin{cases} \dfrac{dt}{ds} = 1 & (15) \\[2mm] \dfrac{d\alpha_1}{ds} = v_{\alpha_1}(\alpha_1, \ldots, \alpha_m) & (16) \\[2mm] \quad \vdots & (17) \\[2mm] \dfrac{d\alpha_m}{ds} = v_{\alpha_m}(\alpha_1, \ldots, \alpha_m) & (18) \\[2mm] \dfrac{dn}{ds} = -\left[\dfrac{\partial v_{\alpha_1}}{\partial \alpha_1} + \cdots + \dfrac{\partial v_{\alpha_m}}{\partial \alpha_m}\right] n(\alpha_1, \ldots, \alpha_m, t). & (19) \end{cases}$$

The characteristic lines of the problem are obtained by solving the Equations 15-18, which depend on the specific formulation of the problem (which

11

gives the actual expressions for $v_{\alpha_1}, \ldots, v_{\alpha_m}$). On the other hand, the formal expression of $n(\alpha_1, \ldots, \alpha_m, t)$ can be written for any problem. It can be obtained dividing Equation 19 by the Equations 16-18. For example, dividing by Equation 16, the result is

$$\frac{dn}{d\alpha_1} = -\frac{1}{v_{\alpha_1}}\Big[\frac{\partial v_{\alpha_1}}{\partial \alpha_1} + \cdots + \frac{\partial v_{\alpha_m}}{\partial \alpha_m}\Big]n$$

where it is possible to separate the variables, so that

$$\frac{dn}{n} = -\frac{1}{v_{\alpha_1}}\Big[\frac{\partial v_{\alpha_1}}{\partial \alpha_1}\Big]d\alpha_1 + \cdots - \frac{1}{v_{\alpha_1}}\Big[\frac{\partial v_{\alpha_m}}{\partial \alpha_m}\Big]d\alpha_1. \tag{20}$$

In the last term, $d\alpha_1/v_{\alpha_1}$ can be rewritten using

$$\frac{d\alpha_1}{v_{\alpha_1}} = \frac{d\alpha_j}{v_{\alpha_j}},$$

with α_j one of the m coordinates. Equation 20 becomes

$$\frac{dn}{n} = -\frac{1}{v_{\alpha_1}}\Big[\frac{\partial v_{\alpha_1}}{\partial \alpha_1}\Big]d\alpha_1 + \cdots - \frac{1}{v_{\alpha_m}}\Big[\frac{\partial v_{\alpha_m}}{\partial \alpha_m}\Big]d\alpha, \tag{21}$$

that can be easily integrated into

$$\log(n) = -\log(v_{\alpha_1}) + \cdots - \log(v_{\alpha_m}) + k$$

where k is a constant of integration. Finally,

$$n = \frac{K^*}{\prod_j^m v_{\alpha_j}}. \tag{22}$$

K is a constant ($K^* = e^k$) that is obtained from the initial condition at $t = 0$ $n_0(\alpha_1, \ldots, \alpha_m) = n(\alpha_1, \ldots, \alpha_m, t = 0)$ as

$$K^* = n_0(\tilde{\alpha}_1, \ldots, \tilde{\alpha}_m) \prod_j^m v_{\alpha_j}(\tilde{\alpha}_1, \ldots, \tilde{\alpha}_m).$$

12

where $\tilde{\alpha}_j$ indicates the function obtained by inverting the characteristic lines G at initial time $t = 0$. So, for example, if from Equations 15-16 it is possible to write the characteristic line for α_j

$$G(\alpha_j, t) = f(\alpha_j) + g(t)$$

then

$$\tilde{\alpha}_j = f^{-1}(G(\alpha_j, t)),$$

with f^{-1} inverse of f.

In the next sections, the continuity equation in multiple dimensions will be applied to three different cases. Firstly, in Section 4 it is used to model the effect of the Earth's oblateness, i.e., the evolution from the ellipsoid (Figure 1a) to the band (Figure 1c). Secondly, in Section 5 it is used to include the distribution in area-to-mass ratio A/M of the fragments for the propagation under the drag effect. Thirdly, in Section 6 it is used to include the distribution in eccentricity, also in this case, for the propagation under the drag effect, once the band is formed.

4. Modelling of the effect of the Earth's oblateness

As discussed in the previous sections, the Earth's oblateness is the dominant perturbation on the fragment cloud evolution before the band formation (Figure 1). The long-term effect of zonal spherical harmonics of the second order J_2 on the orbital parameters can be written as in Vallado (2013)

$$\dot{\Omega} = -\frac{3}{2} J_2 \frac{R_E^2}{p^2} \bar{n} \cos i \tag{23}$$

$$\dot{\omega} = \frac{3}{2} J_2 \frac{R_E^2}{p^2} \bar{n} (2 - \frac{5}{2} \sin^2 i). \tag{24}$$

where R_E is the Earth's radius, p is the semi-latus rectum of the orbit $p = a(1 - e^2)$, $\bar{n}$ is the mean motion $\bar{n} = \sqrt{\mu/a^3}$, and i is the orbit inclination.

The continuity equation can be applied to model this phase of the cloud

13

evolution by writing the problem in the phase space defined by the semi-major axis (a), the longitude of the ascending node (Ω) and the argument of the perigee (ω). Three possible formulations are possible. In the first case, it is assumed that the effect of drag can be neglected and the spreading of the cloud is evaluated only on the angles ω and Ω. In the second case, the effect of drag is consideridered, so that the cloud density is function not only of the two angels, but also of the semi-major axis. Finally, a third approach is presented where only one angle and the semi-major axis are used as variables of the problem.

4.1. Earth's oblateness only

For simplicity, it is assumed that the effect of drag can be neglected during the initial phase of the cloud evolution, which usually lasts a couple of months. This assumption follows the *phased approach* proposed by McKnight (1990) to study space debris cloud evolution as explained in Section 1. This approach was adopted, for example, by Jehn (1991) and Ashenberg and Broucke (1993) to describe how the debris cloud spreads under the effect of the Earth's oblateness, without considering other perturbations. Introducing the approximation that drag can be neglected, the variation of the semi-major axis is null ($v_a = 0$). Nevertheless, the information on the distribution of a is required to calculate the variation of Ω and ω as in Equations 23 and 24. Introducing

$$\lambda = \frac{3}{2}\sqrt{\mu}J_2 R_E^2,$$

the expressions of the variation of the parameters are

$$
\begin{cases}
v_{\alpha_1} = v_a = 0 & (25) \\
v_{\alpha_2} = v_\Omega = -\dfrac{\lambda}{a^{7/2}}\cos i & (26) \\
v_{\alpha_3} = v_\omega = \dfrac{\lambda}{a^{7/2}}\left(2 - \dfrac{5}{2}\sin^2 i\right), & (27)
\end{cases}
$$

14

Since a is constant, the characteristic lines are easily found as

$$
\begin{cases}
G_a(a,t) = a \\
G_\Omega(\Omega,t) = \Omega + \dfrac{\lambda}{a^{7/2}}\cos i\, t \\
G_\omega(\omega,t) = \omega - \dfrac{\lambda}{a^{7/2}}(2 - \dfrac{5}{2}\sin^2 i)t
\end{cases}
$$

that are of the form

$$
G(\alpha,t) = f(\alpha) + g(t)
$$

as introduced in Section 2. As f, in this case for all the three variables, is simply the identity, the expressions obtained inverting the characteristics at the initial time are identical to the characteristics, so

$$
\begin{cases}
\tilde{a} = G_a(a,t) \\
\tilde{\Omega} = G_\Omega(\Omega,t) \\
\tilde{\omega} = G_\omega(\omega,t)
\end{cases}
$$

The density of the cloud can be written as in Equation 22

$$
n(a,\Omega,\omega,t) = n_0(\tilde{a},\tilde{\Omega},\tilde{\omega})\frac{v_\Omega(\tilde{a})v_\omega(\tilde{a})}{v_\Omega(a)v_\omega(a)};
$$

as a is constant, also v_Ω and v_ω can be simplified and therefore

$$
n(a,\Omega,\omega,t) = n_0(a,\tilde{\Omega},\tilde{\omega}). \tag{28}
$$

The dependence of $\tilde{\Omega}$ and $\tilde{\omega}$ on t is linear, so n is computed extremely easily as it corresponds to a simple translation of the domain of the initial conditions.

4.2. Earth's oblateness and atmospheric drag (3D)

If the drag effect is considered, the variation of the semi-major axis is not null. As explained in Section 2, the radial velocity of a fragment due to drag

15

can be expressed as in Equation 3

$$v_r = -\varepsilon\sqrt{r}\exp\Big(-\frac{r - R_H}{H}\Big);$$

also in this case, the hypothesis of circular or quasi circular orbits is kept, so $r \approx a$. Therefore, Equation 3 can be used to express the variation of the semi-major axis substituting r with a. The expressions for the other parameters (Ω, ω) are unchanged with respect to Equations 26 and 27, so the system of ODEs is

$$\begin{cases} \dfrac{dt}{ds} = 1 & (29) \\[2mm] \dfrac{da}{ds} = -\varepsilon\sqrt{a}\exp\Big(-\dfrac{a - R_H}{H}\Big) & (30) \\[2mm] \dfrac{d\Omega}{ds} = -\dfrac{\lambda}{a^{7/2}}\cos i & (31) \\[2mm] \dfrac{d\omega}{ds} = \dfrac{\lambda}{a^{7/2}}(2 - \dfrac{5}{2}\sin i^2) & (32) \\[2mm] \dfrac{dn}{ds} = -\Big[\dfrac{\partial v_a}{\partial a} + \dfrac{\partial v_\Omega}{\partial \Omega} + \dfrac{\partial v_\omega}{\partial \omega}\Big]n(a, \Omega, \omega, t). & (33) \end{cases}$$

The characteristic for a is the one already obtained for r starting from the expression for v_r as in Equation 3, so

$$G_a(a, t) = \exp\Big(\frac{a - R_H}{H}\Big) + \varepsilon\frac{\sqrt{R_H}}{H}t;$$

obtained, as before, with the approximation $\sqrt{a} \approx \sqrt{R_H}$.

The second characteristic of the system is obtained by dividing Equation 31 by Equation 30

$$\frac{d\Omega}{da} = \frac{v_\Omega}{v_a} = \frac{\lambda}{\varepsilon}\frac{\exp\Big(\frac{a - R_H}{H}\Big)}{a^4}$$

whose solution can be expressed as

$$G_\Omega(\Omega, a) = \Omega - \frac{\lambda}{\varepsilon}\cos i\Big[\Gamma(a) - \Gamma(a_0)\Big]$$

as already obtained by McInnes (1994). We take here the occasion to write

16

explicitly $\Gamma(a)$ to amend a typo in the original paper

$$\Gamma(a) = \frac{-\exp\left(\frac{a-R_H}{H}\right)H\left(2H^2 + Ha + a^2\right) + r^3 \exp -\frac{R_H}{H}\text{Ei}\left[\frac{a}{H}\right]}{6H^3 a^3}$$

where $\text{Ei}(z)$ is the exponential integral function, defined as

$$\text{Ei}(z) = -\int_{-z}^{\infty} \frac{\exp(-u)}{u}\,du.$$

As ω and Ω have the same dependence on a, also the characteristic for ω is expressed through the function Γ and only the constant factor is different. In particular, the expression for ω is

$$G_\omega(\omega, a) = \omega + \frac{\lambda}{\varepsilon}(2 - \frac{5}{2}\sin i^2)\Big[\Gamma(a) - \Gamma(a_0)\Big].$$

Therefore, also in this case is possible to write an explicit expression for n

$$n(a, \Omega, \omega, t) = n_0(\tilde{a}, \tilde{\Omega}, \tilde{\omega})\frac{v_a(\tilde{a})v_\Omega(\tilde{a})v_\omega(\tilde{a})}{v_a(a)v_\Omega(a)v_\omega(a)} \tag{34}$$

with

$$\begin{cases} \tilde{a} = R_H + H\log\left(G_a(a, t)\right) \\ \tilde{\Omega} = G_\Omega(\Omega, \tilde{a}) \\ \tilde{\omega} = G_\omega(\omega, \tilde{a}). \end{cases}$$

Note that here the initial condition is not simply translated across the domain, but, as the semi-major axis decreases with time, the initial distribution is modified with time as expressed by Equation 34.

4.3. Earth's oblateness and atmospheric drag (2D)

If the purpose of the method is to obtain the long term evolution of the cloud, the scope of the description of the effect of the Earth's oblateness is to estimate when the band (Figure 1c) is formed and to have at the time a faithful representation of the fragment distribution with the orbital parameters. This can be achieved with a simplified expression of Equation 34 that considers the

17

semi-major axis a and only one angle between Ω and ω. The angle to be chosen is the slowest in spreading during the band formation. Following Ashenberg (1994), for each altitude and inclination of the parent orbit is possible to know *a priori* which angle drives the band formation. For example, if Ω is the relevant angle to determine the time for band formation, the equations for this case are the same as the 3D case, but as ω can be disregarded, the expression for n is simplified to

$$n(a, \Omega, t) = n_0(\tilde{a}, \tilde{\Omega}) \frac{v_a(\tilde{a}) v_\Omega(\tilde{a})}{v_a(a) v_\Omega(a)}.$$

4.4. Results

The analytical modelling of the initial phase of the cloud evolution was validated through the comparison with the results obtained with the numerical integration, using PlanODyn as propagator. The domain is divided into cells with width equal to $25\,\mathrm{km}$ in semi-major axis and 3.6 degrees in the two angles ω and Ω. The number of fragments N_F in each cell, according to the different propagator, is counted and compared. The cloud analysed in the following is generated by a breakup in a circular orbit with altitude equal to $800\,\mathrm{km}$ and inclination equal to 30 degrees. The cloud evolution is followed from the breakup up to 150 days later, when the transition to the band can be considered complete.

Figures 3, 4, 5 show respectively the evolution of the distributions in a, ω, Ω for the proposed analytical methods and for the numerical propagation. The accuracy in the description of the distribution in a is the most relevant figure to consider as it has a direct impact on the estimated value of the spatial density. From Figure 3 one can observe how neglecting the effect of drag leads to an overestimation of the number of objects with low semi-major axis. Two indicators are used to estimate the method accuracy. The first, $\mathrm{err}_{\mathrm{tot}}$, is a metric of the global accuracy of the method and measures the relative error of the total number of fragments obtained by integrating the density curve in altitude (h)

$$\mathrm{err}_{\mathrm{tot}} = \frac{|\int n_A \, dh - \int n_N \, dh|}{\int n_N \, dh}.$$
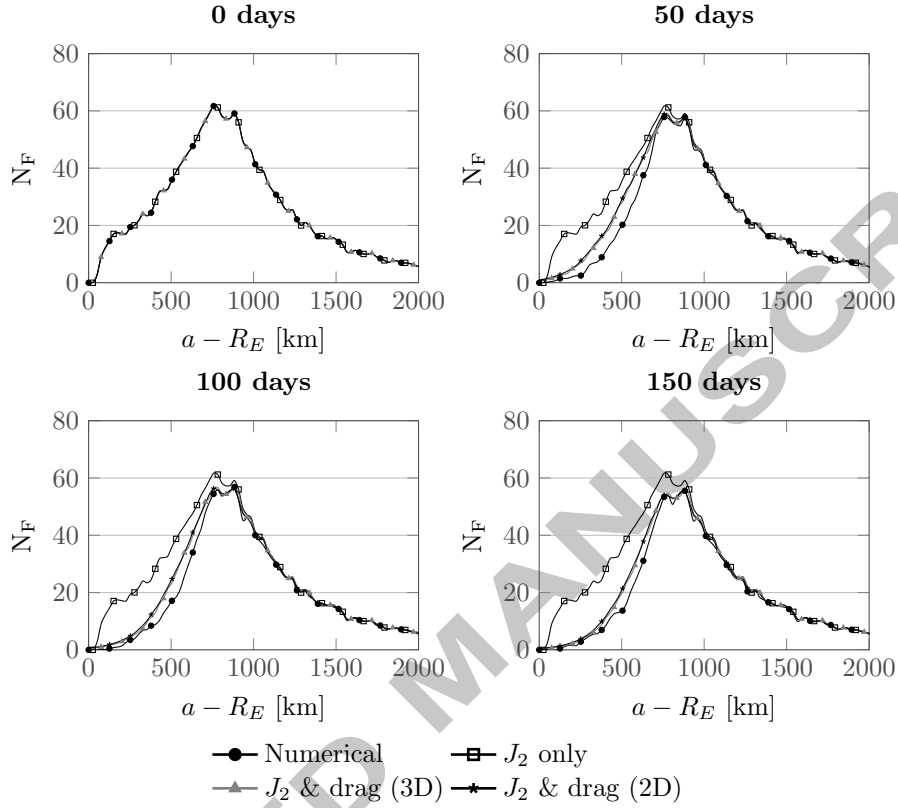
18

Figure 3: Evolution of the distribution of the semi-major axis, for a fragmentation at $800\,\mathrm{km}$ and $i = 30°$, from the fragmentation to 150 days after the event.

The second, $\mathrm{err}_{\mathrm{peak}}$, is a local metric as it measures the relative error on the peak, comparing the maximum density value for the analytical n_A and numerical propagation n_N,

$$\mathrm{err}_{\mathrm{peak}} = \frac{|\max\left(n_A\right) - \max\left(n_N\right)|}{\max\left(n_N\right)}.$$

Table 2 shows the value of the two indicators for the different propagation methods. It appears clearly that the assumption that drag can be neglected in the first phase of the cloud evolution is not valid.

Figure 4 shows how the spreading of ω is well captured, but, as expected, neglecting drag brings also in this case to an overestimation of the number of
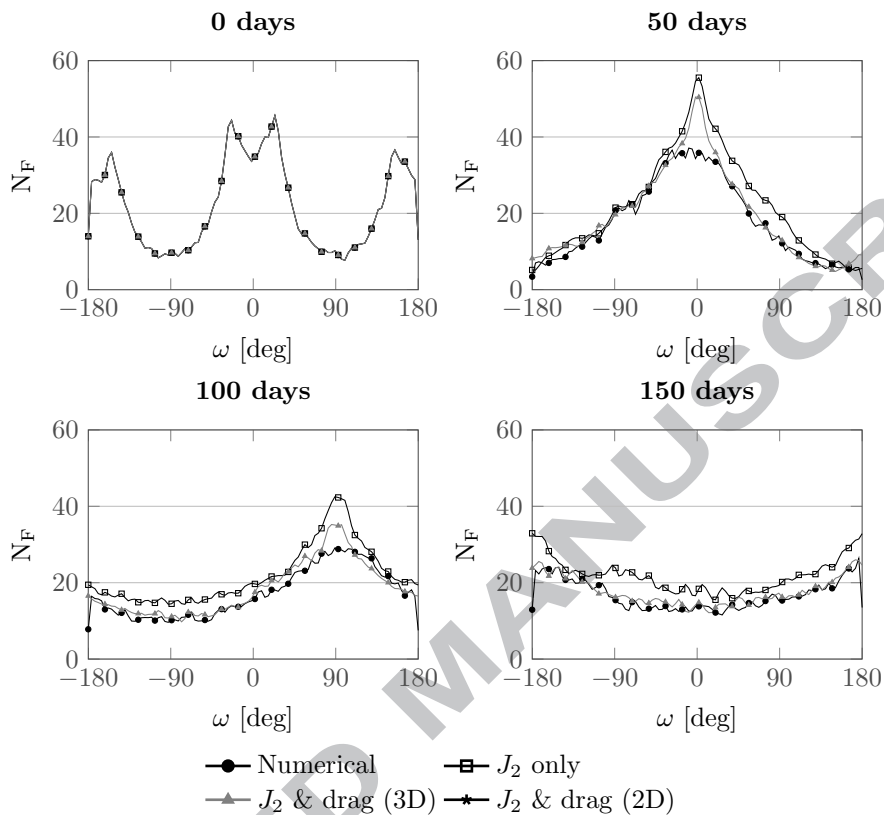
19

Figure 4: Evolution of the distribution of the argument of the perigee, for a fragmentation at $800 \, \text{km}$ and $i = 30°$, from the fragmentation to 150 days after the event.

fragments. Figure 5 shows the evolution of the distribution of Ω. Observe that in this case the initial condition was modified substituting the real initial distribution where all fragments have $\Omega = 0$ with a Gaussian distribution. This was done to avoid numerical issues such as instabilities, even if some anomalous peaks are still presents (e.g. the one at -5 degrees at $t = 150$ days).

In terms of computational time, all the analytical approaches are much faster than the numerical propagation. The average running time over ten simulations, as measured by Matlab built-in functions and for a PC with four CPUs at 3.4GHz, is reported in Table 2; for the numerical propagation the average
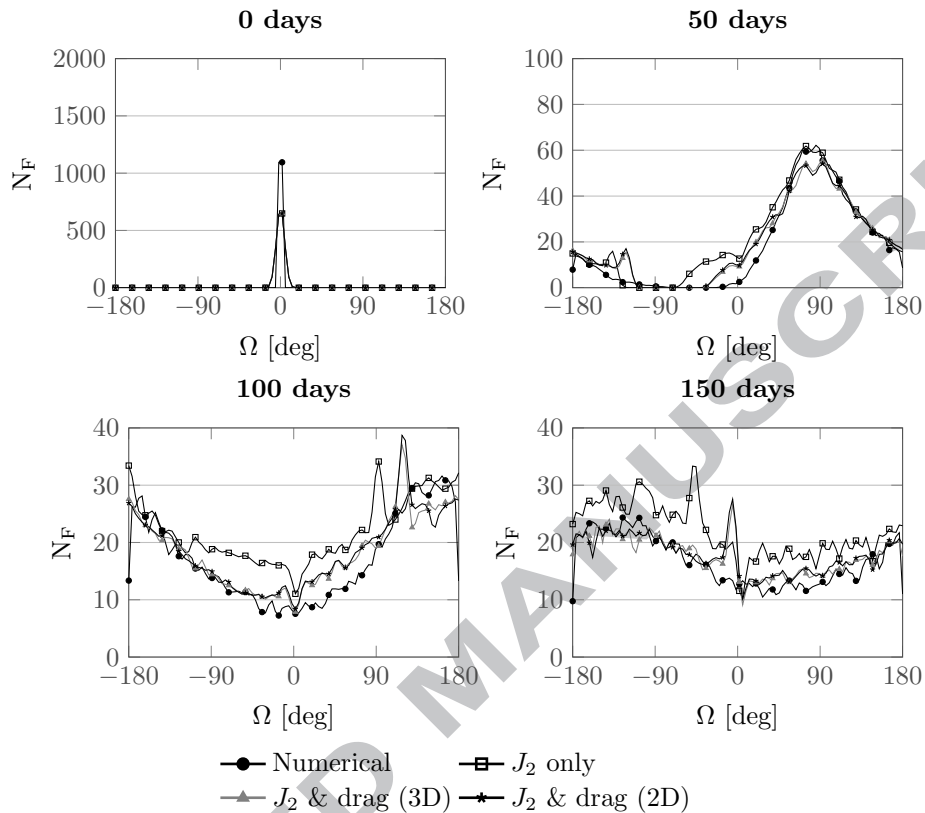
20

Figure 5: Evolution of the distribution of the longitude of the ascending node, for a fragmentation at $800 \, \text{km}$ and $i = 30°$, from the fragmentation to 150 days after the event.

computational time is equal to $55 \, \text{s}^2$. Including drag doubles the computational time , but the numbers are so low that there is not a practical convenience in using the model with the Earth's oblateness only. On the other hand, reducing the number of parameters gives a larger speed-up while keeping a better level of accuracy.

Given the performance both in terms of accuracy and computational time, the application of the continuity equation to the initial phase of the cloud evolution appears promising. Future work will aim to use the analytical propagation

---

[2]The fact that the computational time is longer in this case than for the long term simulations studied in Section 6 is due to the fact that in the short time simulated here only a few fragments decay.

Table 2: Accuracy and computational time t_c for the three approaches to the modelling of the initial evolution of a fragment cloud.

Method	$\mathrm{err}_{\mathrm{tot}}$	$\mathrm{err}_{\mathrm{peak}}$	t_c [s]
Earth's oblateness only	0.33	0.38	0.18
Earth's oblateness + atmospheric drag (2D)	0.07	0.11	0.08
Earth's oblateness + atmospheric drag (3D)	0.06	0.08	0.37

to describe the spreading of the angles ω and Ω and asses when the band is formed. Another application could be the description of the cloud density in coordinates such as geocentric distance, longitude and latitude to allow for an analytical estimation of the collision probability also before the band formation.

5. Modelling of the A/M distribution

In the 1D approach with the continuity equation for the description of drag effect presented in Section 2, all the constants of the problem are collected in the parameter ε defined in Equation 4

$$\varepsilon = \sqrt{\mu}\frac{c_D A}{M}\rho_0;$$

however, A/M is not the same for all the fragments in a debris cloud.

Figure 6 shows the distribution of A/M obtained by one simulation with the NASA breakup model a non-catastrophic collision with energy equal 100 kJ. According to the model, the distribution of A/M is a log-normal distribution with mean value and standard deviation that depend on the fragment size (Johnson and Krisko, 2001). In particular, the simulated case presents a minimum value equal to $0.0288\,\mathrm{m^2\,kg^{-1}}$, a maximum value of $15.3978\,\mathrm{m^2\,kg^{-1}}$ and a peak of the distribution around $0.4\,\mathrm{m^2\,kg^{-1}}$.

The formulation by McInnes (1993) does not consider this distribution of A/M, which has instead a large impact on the fragment evolution. The novel extension to 2D explained in Section 3 can be applied to consider the area-to-mass ratio as an additional parameter in the continuity equation, thus improving the description of the drag effect. The equation that describes the evolution of
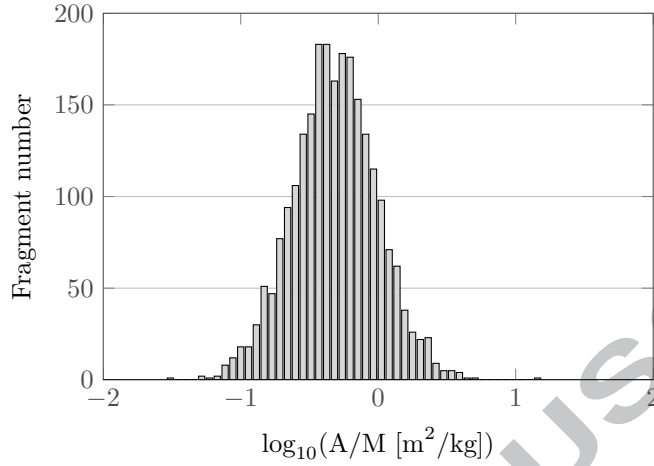
22

Figure 6: Area-to-mass ratio distribution for a non-catastrophic collision of 100 KJ.

A/M is simply

$$\frac{dA/M}{dt} = 0,$$

which means that the shape and the attitude of the fragments does not change with time, while the evolution of the fragment distance is described by Equation 6.

In this case, using the same notation as in Section 3,

$$\alpha_1 = r$$
$$\alpha_2 = A/M$$
$$v_{\alpha_1} = v_r = -\varepsilon\sqrt{R}\exp\left(-\frac{r}{H}\right)$$
$$v_{\alpha_2} = v_{A/M} = 0$$
$$\tilde{\alpha}_1 = \tilde{r} = R_H + H\log\left(G(r,t)\right)$$
$$\tilde{\alpha}_2 = \tilde{A/M} = (A/M)$$

where the expression of the characteristic for r, $G_r(r,t)$, is the same as in Equation 11

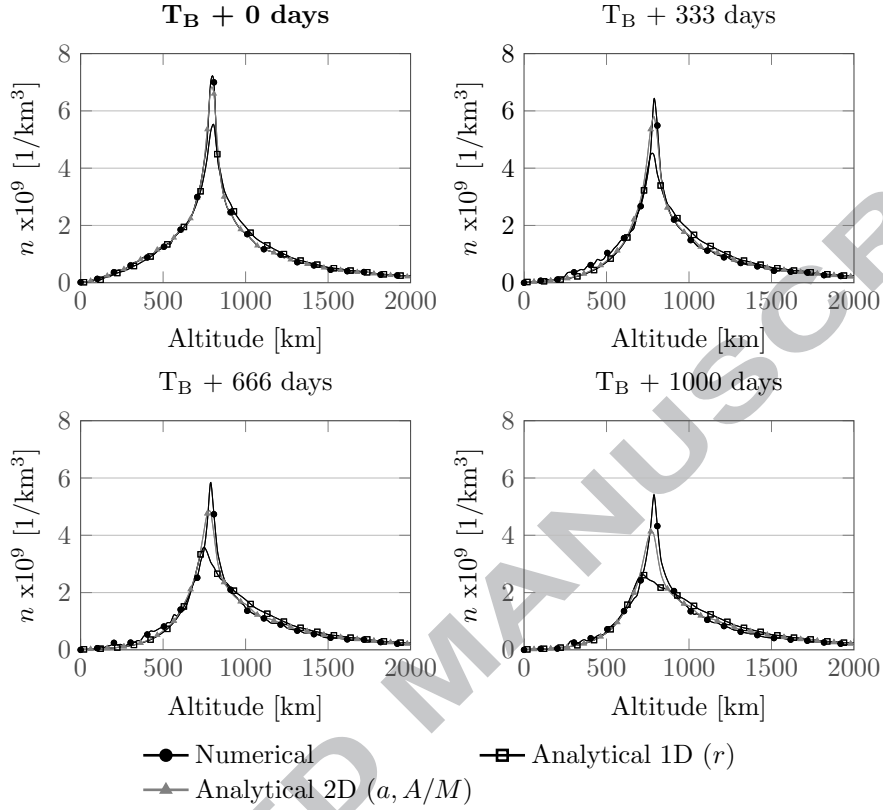$$G_r(r,t) = \exp\left(\frac{r - R_H}{H}\right) + \varepsilon\frac{\sqrt{R_H}}{H}t$$

23

Figure 7: Evolution of the cloud density (n) profile as a function of time after the band formation T_B ($T_B = 95$ days) for a fragmentation at 800 km, $i = 0$ degrees.

and v_r depends on A/M through ε as shown in Equation 4. The final expression for the fragment density, applying Equation 22, is

$$n(r, A/M, t) = n_0(r, A/M) \frac{v_r(\tilde{r}, A/M)}{v_r(r, A/M)}.$$

5.1. Results

Figure 7 compares the results of the analytical propagation with the output of the numerical one. The results are expressed in terms of spatial density, which in the case of the numerical propagation is obtained counting the number of objects in spherical shells with thickness equal to 20 km. Figure 7 shows how the 2D formulation is able to follow very well the evolution of the cloud and

24

represents a significant improvement of the 1D approach for treating A/M. In particular, after 1000 days from the band formation, the relative error on the peak $\mathrm{err_{peak}}$ is equal to 49% for the 1D method and 20% for the 2D one.

However, it has to be noted that treating A/M as an additional dimension of the problem increases its complexity. In particular, here it is possible to keep a 1D formulation of the problem and divide the fragments into N_b bins in area-to-mass ratio, for example defining the bins in such a way that each one contains the same number of fragments at the band formation (Letizia et al., 2015a). For each bin, an average ε_j is assumed and the corresponding density n_j is obtained using Equation 12; all the partial densities n_j are summed to obtain the global cloud density n

$$n(r,t) = \sum_{j}^{N_b} n_j(r,t).$$

Figure 8 shows the density at 1000 days for a fragmentation at 800 km for different formulations of the problem: both including 5 and 10 bins is possible to obtain a result similar to the 2D approach around the peak area. Additional analysis has shown that 10 is the optimal bins number in the trade-off between computational time and relative error (Letizia et al., 2015a).

6. Modelling of the eccentricity distribution

The method explained in Section 2 is based on the hypothesis that the fragments are on circular orbits: this allows obtaining a full analytical solution for the spatial density evolution under the drag effect. However, this also limits the applicability of the method to altitudes equal to and higher than 800 km. In fact, at lower altitudes, even in case of a small value of eccentricity, the atmosphere density changes so largely along one single orbit that Equation 3 is not accurate anymore Letizia et al. (2015a). For this reason, the eccentricity should be included in the propagation. In particular, the problem is here formulated in terms of the evolution of the debris cloud in the phase space defined by
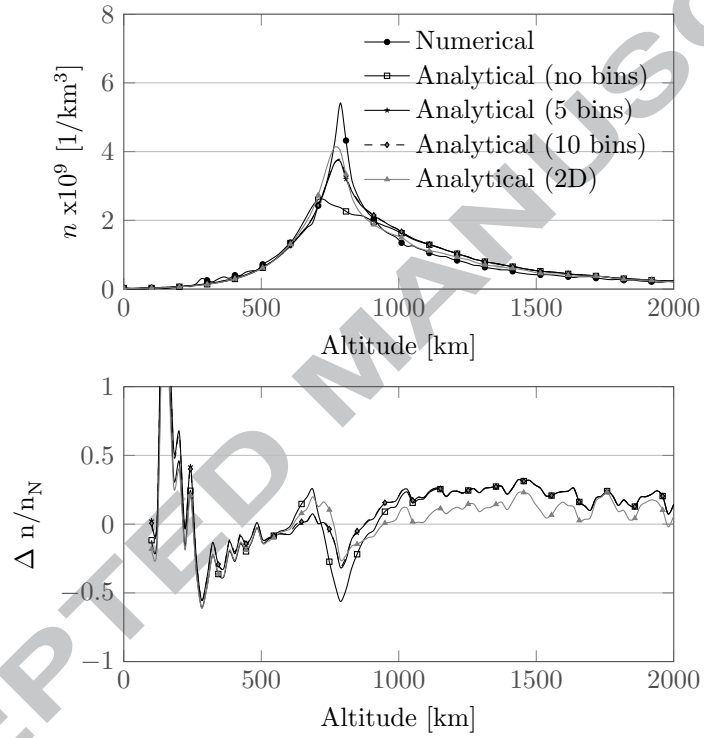
25

Figure 8: Density profile at 1000 days after the band formation T_B ($T_B = 95$ days) for a fragmentation at $800\,\mathrm{km}$, $i = 0$ degrees for different propagators and relative error measured with respect to the value obtained with the numerical propagation n_N.

26

the semi-major a and the eccentricity e. In this case, the cloud spatial density in [1/km^3] is computed *a posteriori* through expressions such as the ones by Kessler (1981) or Sykes (1990).

In order to apply the equations obtained in Section 3, an expression for the rate of variation of a and e, respectively v_a and v_e, is required. They both can be obtained from the expression for the variation of the orbital parameters in one orbit

$$\Delta a = -2\pi \frac{c_D A}{M} a^2 \rho_{\text{ref}} \exp\left(-\frac{a - R_H}{H}\right)\left[I_0 + 2eI_1 + O(e^2)\right] \tag{35}$$

$$\Delta e = -2\pi \frac{c_D A}{M} a \rho_{\text{ref}} \exp\left(-\frac{a - R_H}{H}\right)\left[I_1 + \frac{e}{2}(I_0 + I_2) + O(e^2)\right]; \tag{36}$$

derived by King-Hele King-Hele (1987) for orbits whose eccentricity is between 0.01 and 0.1. It is assumed that the other orbital parameters are unchanged under the hypothesis the Earth's rotation is neglected.

I_n indicates the modified Bessel function of the first kind and order n with argument $z = ae/H$, where H is the scale height coming from the exponential model of the atmosphere; $I_n(z)$ can be defined by the contour integral

$$I_n(z) = \frac{1}{2\pi i} \oint e^{(z/2)(t+1/t)} t^{-n-1} \, dt; \tag{37}$$

for $n \in \mathbb{Z}$ the definition can be simplified into

$$I_n(z) = \frac{1}{\pi} \int_0^\pi e^{z \cos \theta} \cos n\theta \, d\theta. \tag{38}$$

The expression of the velocities is therefore

$$v_a = -\sqrt{\mu a} \frac{c_D A}{M} \rho_0 \exp\left(-\frac{a - R_H}{H}\right) f(a, e, H)$$
$$v_e = -\sqrt{\frac{\mu}{a}} \frac{c_D A}{M} \rho_0 \exp\left(-\frac{a - R_H}{H}\right) g(a, e, H) \tag{39}$$

where

$$f(a, e, H) = I_0 + 2eI_1 + O(e^2)$$
$$g(a, e, H) = I_1 + \frac{e}{2}(I_0 + I_2) + O(e^2). \tag{40}$$

27

Introducing the parameter ε as in Equation 4, the resulting system of equations is

$$\begin{cases} \dfrac{dt}{ds} = 1 & (41) \\[2mm] \dfrac{da}{ds} = -\varepsilon\sqrt{a}\exp\Big(-\dfrac{a-R_H}{H}\Big)f(a,e,H) & (42) \\[2mm] \dfrac{de}{ds} = -\dfrac{\varepsilon}{\sqrt{a}}\exp\Big(-\dfrac{a-R_H}{H}\Big)g(a,e,H) & (43) \\[2mm] \dfrac{dn}{ds} = -\Big[\dfrac{\partial v_a}{\partial a} + \dfrac{\partial v_e}{\partial e}\Big]n(a,e,t) & (44) \end{cases}$$

that, however, does not admit an analytical solution. Two approximations are, therefore, introduced:

$$\sqrt{a} \approx \sqrt{R_H} \tag{45}$$

and

$$f(a,e,H) \approx f(R_H,e,H) \qquad g(a,e,H) \approx g(R_H,e,H); \tag{46}$$

the impact of these approximations on the accuracy of the trajectory evolution was verified and considered acceptable, as shown in Figure 9. It shows the relative error on the semi-major axis err_a and on the eccentricity err_e

$$\mathrm{err}_a = \frac{\tilde{a} - a_N}{a_N} \qquad \mathrm{err}_e = \frac{\tilde{e} - e_N}{e_N}$$

where $(\tilde{a}, \tilde{e})$ are the values of the orbital parameters obtained introducing the approximations in Equations 45 and 46, and (a_N, e_N) are the values obtained from the numerical propagation, without any approximation. In all cases shown in Figure 9, the semi-major axis is set equal to $R_E + 700$ km while four different values of eccentricity are considered. The error is very low for the first two case ($e = 0.010$ and $e = 0.037$), whose curves lay on the x-axis in Figure 9. In general, the error is lower than 1% both for the semi-major axis and for the eccentricity for all the cases except the one with $e = 0.092$, whose perigee is equal to 50 km, the threshold value below which the fragments are considered to being re-entering. These fragments are likely to re-enter much faster than the other ones, so also their impact on the propagation of the cloud is limited
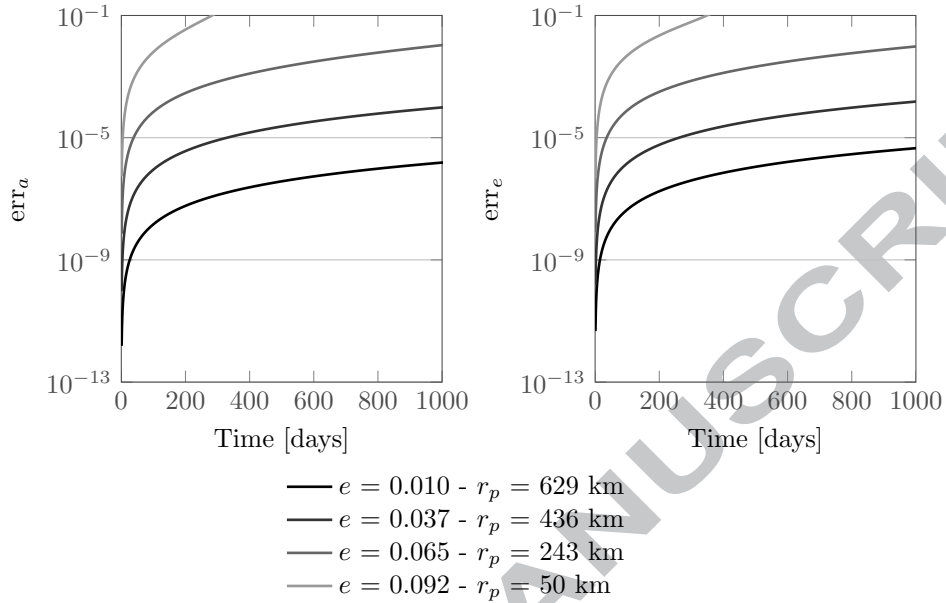
28

Figure 9: Relative error on the semi-major axis a and on the eccentricity e resulting from the approximation in Equation 46 for fixed semi-major axis equal to $R_E + 700$ km and different values of eccentricity.

in time.

However, also with the approximations in Equations 45 and 46 it was not possible to obtain an analytical solution as the complexity of the problems derives from the fact that the evolution in a and e are coupled through the Bessel functions. One tentative to approximate the problem is to decouple the equations by assuming a constant eccentricity $v_e = 0$. This is still a strong hypothesis on the eccentricity, but compared to the 1D approach, the 2D formulation takes into account the eccentricity distribution and uses this information to correct the evolution of the semi-major axis, although its derivative is considered to be null.
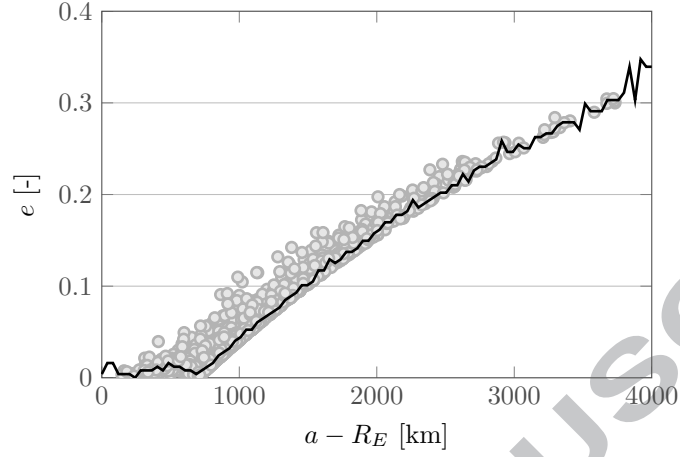
29

Figure 10: Distribution of semi-major axis and eccentricity, for a fragmentation at 700 km, at the band formation (92 days after the fragmentation).

Therefore, the problem is solved setting

$$\alpha_1 = a \tag{47}$$

$$\alpha_2 = e \tag{48}$$

$$v_{\alpha_1} = v_a = -\sqrt{\mu R_H} \frac{c_D A}{M} \rho_0 \exp\left(-\frac{a - R_H}{H}\right) f(R_H, \tilde{e}(a), H) \tag{49}$$

$$v_{\alpha_2} = v_e = 0 \tag{50}$$

$$\tilde{\alpha}_1 = \tilde{a} = H \log\left[\left(\exp\left(\frac{a - R_H}{H}\right) + \varepsilon f(R_H, \tilde{e}(a), H) \frac{\sqrt{R_H}}{H} t\right] \tag{51}$$

$$\tilde{\alpha}_2 = \tilde{e} = e. \tag{52}$$

Note that an heuristic was adopted in Equation 49, introducing $\tilde{e}(a)$ that expresses a reference value of the eccentricity for each value of the semi-major axis. This means that, given a value of the semi-major axis a_j, $\tilde{e}(a_j)$ is the constant value associated with it. The value of $\tilde{e}(a)$ can be obtained starting from the initial distribution $n_0(a, e)$: the function e_0 is built assigning to each value of the semi-major axis the value of eccentricity where the density is maximum;

30

for example, for $a = a_j$

$$\tilde{e}(a_j) = e_j : n_j = n_0(a_j, e_j) = \max(n_0(a_j, e)).$$

The resulting function for the case at 700 km is shown in Figure 10.

6.1. Results

The result of the numerical propagation in terms of density in the phase space is shown in Figure 11a: the domain is divided into cells with width equal to 25 km in semi-major axis and 0.005 in eccentricity; the plot shows the number of fragments N_F in each cell. The plot on the left refers to the moment of band formation and it is easy to recognise the v-shaped distribution of eccentricity with semi-major axis, which is an alternative representation of the well known Gabbard diagram (Portree and Loftus, 1999). The v-shaped curve is centred on the altitude of the parent orbit: the leg on the left represents the fragments whose orbits have the fragmentation location as apogee, the leg on the right those with the fragmentation location as perigee. The plot on the right refers instead to the cloud density at 1000 days after the band formation: the number of fragments is reduced and the fragments with low semi-major axis are on circular orbits, therefore one leg of the v-shaped distribution disappears.

The same plots can be obtained also with the analytical approach in 2D (Figure 11b) which provides a distribution of fragments extremely similar to the numerical simulation. The most evident difference in the density after 1000 days from the band formation is that the analytical approach underestimates the number of fragments with $e \approx 0$.

This fact is even clearer from Figure 12 that shows the distributions of semi-major axis and eccentricity for the numerical propagation and for the 2D analytical approach at the different time instants. After 1000 days from the band formation, the distribution of the semi-major axis is well captured (Figure 12); on the other hand, the analytical approach is not able to represent the peak at $e \approx 0$ in the eccentricity distribution. This happens because the analytical

31
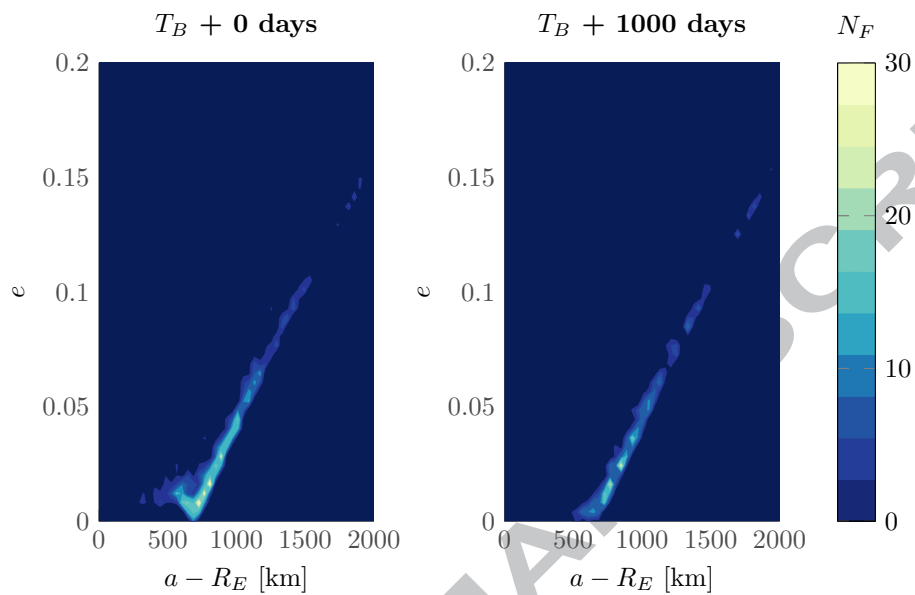
(a) Numerical propagation
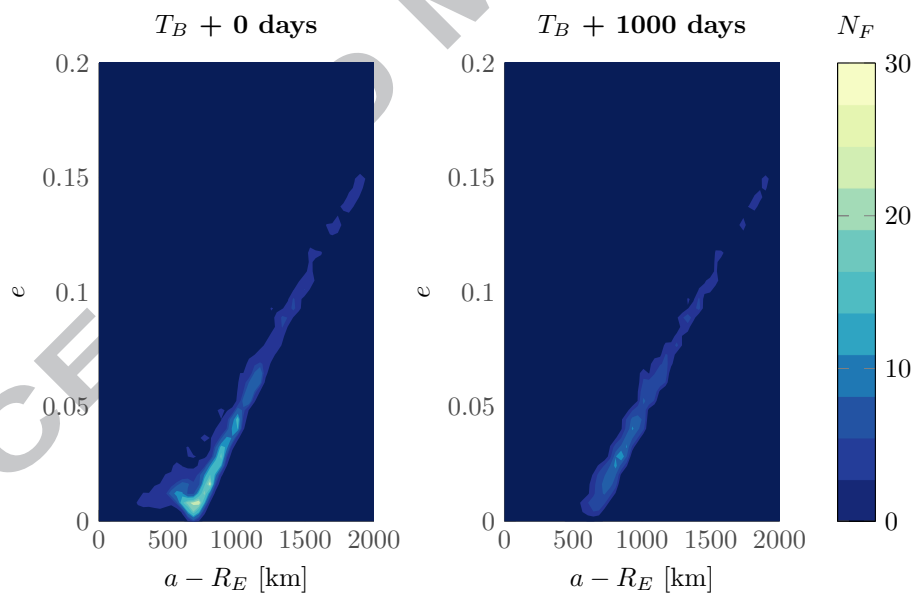
(b) Analytical propagation

Figure 11: Visualisation of cloud density (in number of fragments) at the band formation ($T_B = 92$ days) and after 1000 days for two propagation methods.
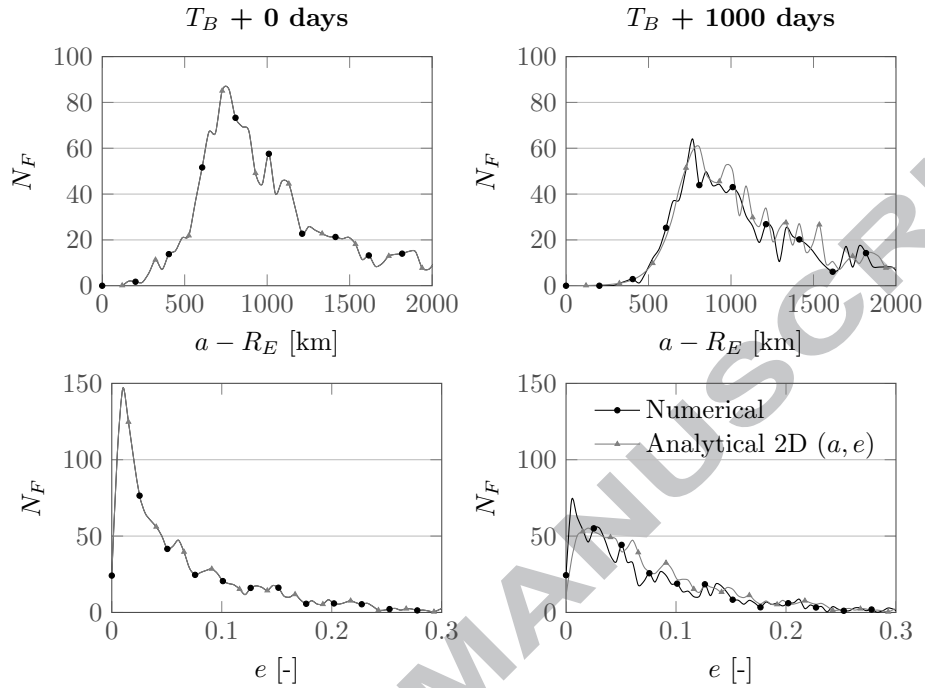
Figure 12: Distribution of semi-major axis and eccentricity, for a fragmentation at 700 km, at the band formation ($T_B = 92$ days) and after 1000 days.

propagation is obtained starting from the equation

$$\frac{de}{dt} = 0$$

so the progressive reduction of eccentricity is lost.

Despite this error, it is possible to see from Figure 13 how the 2D approach represents in any case a remarkable improvement compared to the 1D method used in Letizia et al. (2015a). Figure 13 shows the cloud density profile after 1000 days from the band formation for a fragmentation at six different altitudes. The value of spatial density for the numerical propagation is obtained dividing the altitude in bin with width equal to 25 km, counting the number of fragments in each bin and dividing by the volume of the corresponding spherical shell. For the numerical propagation ten runs of the breakup model were performed to take into account the random parameters within the model.
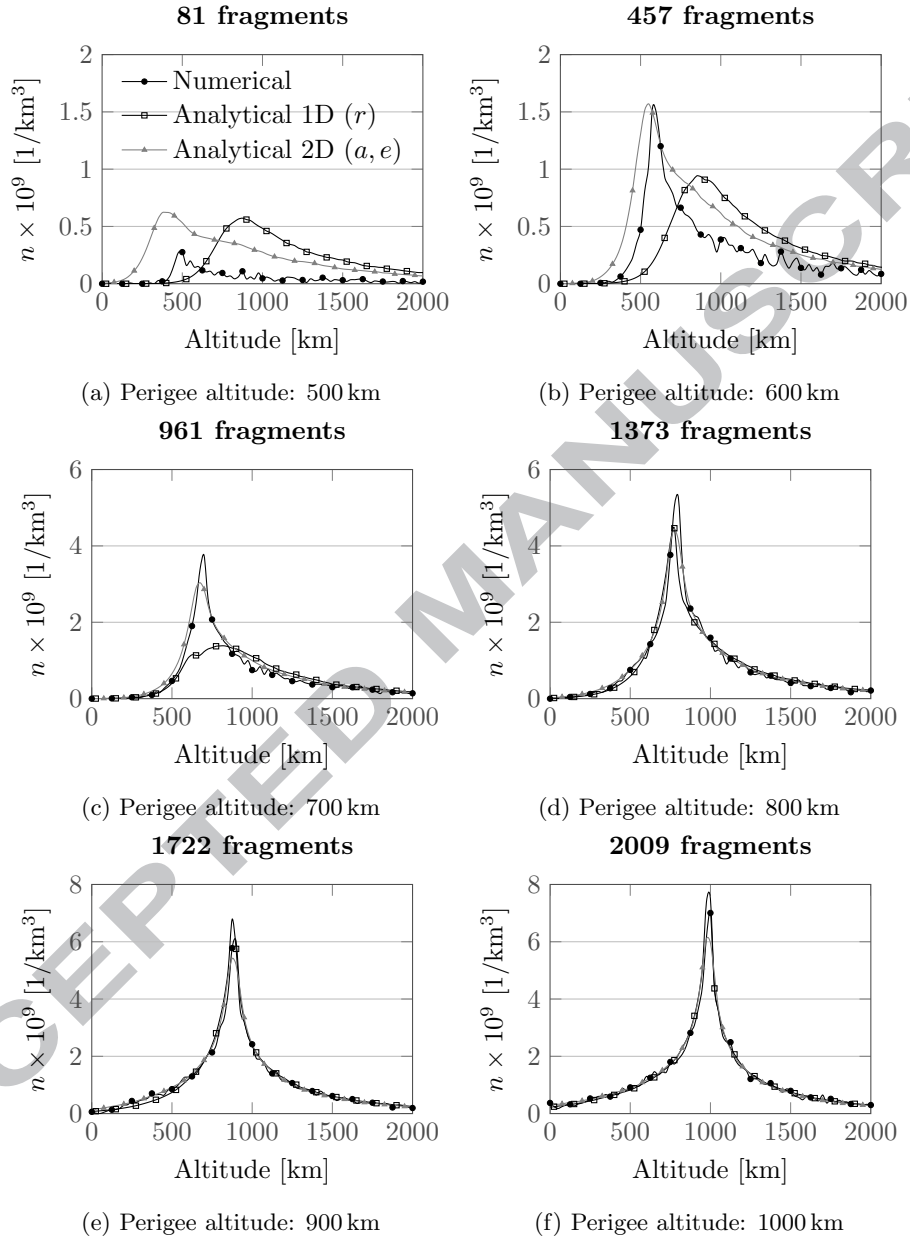
33

81 fragments

457 fragments

(a) Perigee altitude: 500 km

(b) Perigee altitude: 600 km

961 fragments

1373 fragments

(c) Perigee altitude: 700 km

(d) Perigee altitude: 800 km

1722 fragments

2009 fragments

(e) Perigee altitude: 900 km

(f) Perigee altitude: 1000 km

Figure 13: Cloud density after 1000 days from the band formation for six different collision altitudes.

34

At high altitudes the accuracy of the 1D and the 2D formulation is similar. At 700 km only the 2D method is able to identify the correct peak location and the relative error on the peak height is halved. The case of a fragmentation at 600 km shows that even the 2D approach is not able to obtain an accurate prediction of the cloud evolution at such low altitudes. Note, however, that if the fragmentation happens at very low altitude, the number of fragments after 1000 days is very low, so even the use of a continuum approach is questionable for such a limited number of samples.

The relative error on density peak and on the total number of fragments for the methods is plotted in Figure 14. Setting a threshold value at 20%, which corresponds to a good visual agreement between the density profile obtained with the numerical propagation and the one with the analytical one, the 1D approach is applicable above 800 km and the 2D approach instead can be applied from 700 km and the average error on the respective ranges of applicability is similar. This extends the applicability of the method in a such a way that it can be applied along the whole altitude range of the sun-synchronous orbits, where the debris density is the highest and where there are many critical objects in terms of possible future fragmentations.

The improvement in the results is associated with a small increase in the computational time that can be evaluated from Figure 15, which shows the time required to estimate the cloud density 1000 days after the band formation. The measured computational times refer to a PC with 4 CPUs at 3.40 GHz and the numbers in Figure 15 refer to the average over ten runs. All the codes are written in MATLAB and parallelised. The propagation with the 2D formulation requires more than double the time of the 1D (1.34 s compared to 0.66 s), but the computational time is still lower than the numerical propagation. The final step of conversion from the density in the (a, e)-plane into the spatial density in $1/\text{km}^3$ appears quite expensive (2.17 s). One can observe that for applications when the propagation method is used to compute the collision probability for a spacecraft crossing the cloud the value of n is required only at the target altitude, so the computation is faster. On the other hand, when the cloud
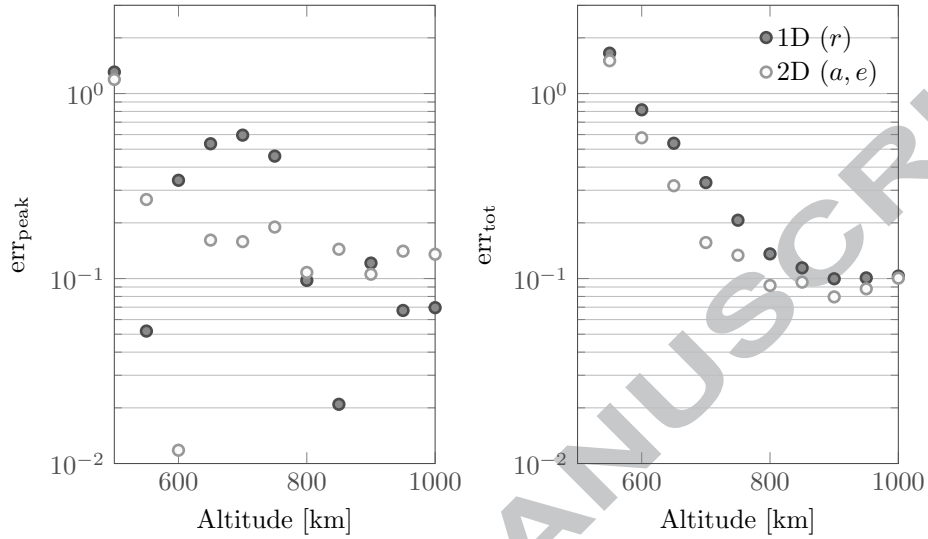
35

Figure 14: Accuracy of the method, measured by the relative error on peak and total fragment number after 1000 days from the band formation, as a function of the fragmentation altitude, for analysed propagation techniques.
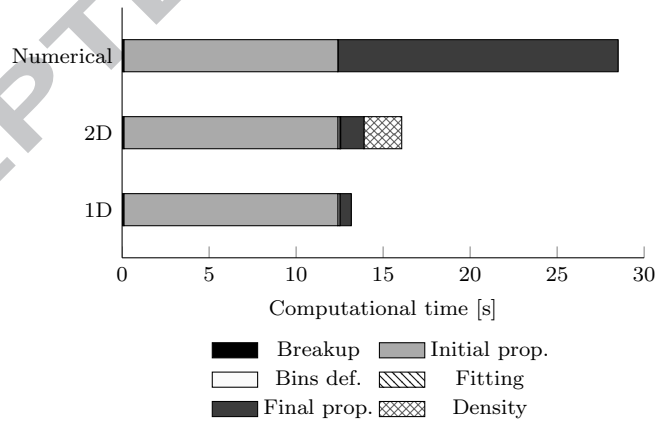

Figure 15: Computational time for a PC with 8 CPUs at 3.40 GHz and the division of the cloud into ten bins in A/M.

36

propagation is used for such application, it is not sufficient to know the state of the cloud at the final time, but a fine time step should be adopted. As at each time step the fit of a 2D function is performed, the operation could be expensive, so future work will investigate alternative implementations. In any case, it is important to highlight that the running time is only a part of the computational effort required by a simulation. The main advantage of the proposed approach is that describing the problem in terms of spatial density instead of studying the position of each objects reduces the required RAM. This means that large fragmentations (e.g. with more than 10000 fragments) can me simulated on normal PCs, without the used of supercomputers.

The saving in the computational time achieved also with the 2D approach suggests that it also can be applied to study many different fragmentation scenarios to understand which conditions affect the most the debris environment and the collision probability for operational spacecraft.

7. Conclusions

Studies on space debris usually refer only to the population of objects larger than 10 cm. Large objects are, indeed, the most dangerous as, in case of collision, they are able to destroy a satellite and to create larger debris cloud. However, also small debris fragments can represent a relevant hazard to operational satellites, but their contribution to the collision risk is often disregarded for two main reasons: the lack of a catalogue with data on single small objects and the requirement for a different approach to propagate them. In fact, the number of small fragments is so large that the *traditional* propagation of all objects is not feasible because it would result into a prohibitive computational effort.

Some models dealt with this issue defining some representative objects that are studied instead of the actual population of small fragments. This work proposes instead a continuous approach based on the description of the fragments dynamics in terms of the evolution of their spatial density. The method was

already applied to describe the evolution of debris clouds under the effect of drag for orbits at minimum 800 km. The long term evolution of the cloud is obtained by applying the continuity equation that, introducing some hypotheses, admits an analytical solution. The possibility of writing an explicit expression for the density, as a function of time and distance, provides a very quick way to describe the small fragments dynamics and their contribution to the collision probability.

Here the method applicability was extended by switching to a 2D formulation where the coordinates are the most relevant parameters of the studied scenario. In this way it was possible to apply the density method to describe also the effect of the Earth's oblateness and the distribution of the area-to-mass ratio and of the eccentricity among the fragments. This last application, in particular, extends the method applicability down to 700 km, so that it can be used to describe the evolution of the fragment clouds originating from all the regions with the highest space debris density, such as sun-synchronous orbits. On the other hand, the possibility of modelling also the effect of the Earth's oblateness suggests that it should be possible to formulate an analytical approach able to follow the debris clouds both in short and in long time-scales.

Acknowledgement

References

Ashenberg, J., 1994. Formulas for the phase characteristics in the problem of low-Earth-orbital debris. Journal of Spacecraft and Rockets 31, 1044–1049. doi:10.2514/3.26556.

Ashenberg, J., Broucke, R., 1993. The effect of the Earth's oblateness on the long-term dispersion of debris. Advances in Space Research 13, 171–174.

Colombo, C., 2015. Long-term evolution of highly-elliptical orbits: Luni-solar perturbation effects for stability and re-entry, in: 25th AAS/AIAA Space Flight Mechanics Meeting. AAS-15-395.

Colombo, C., McInnes, C.R., 2011. Evolution of swarms of smart dust spacecraft, in: New Trends in Astrodynamics and Applications VI, Courant Institute of Mathematical Sciences, New York.

Evans, L., 1998. Partial Differential Equations. Graduate studies in mathematics, American Mathematical Society.

Gor'kavyi, N., 1997. A new approach to dynamical evolution of interplanetary dust. The Astrophysical Journal 474, 496–502. doi:10.1086/303440.

Gor'kavyi, N., Ozernoy, L., Mather, J., Taidakova, T., 1997. Quasi-stationary states of dust flows under Poynting-Robertson drag: New analytical and numerical solutions. The Astrophysical Journal 488, 268–276.

Hoots, F.R., Hansen, B.W., 2014. Satellite breakup debris cloud characterization, in: 24th AAS/AIAA Space Flight Mechanics Meeting, Santa Fe. AAS 14-329.

IADC Steering Committee, 2013. IADC Assessment Report for 2011. Technical Report IADC-12-06. Inter-Agency Space Debris Coordination Committee.

Izzo, D., 2002. Statistical modelling of orbits and its application to trackable objects and to debris clouds. Ph.D. thesis. Università La Sapienza.

Jehn, R., 1991. Dispersion of debris clouds from In-orbit fragmentation events. ESA Journal 15, 63–77.

Johnson, N.L., Krisko, P.H., 2001. NASA's new breakup model of EVOLVE 4.0. Advances in Space Research 28, 1377–1384. doi:10.1016/S0273-1177(01)00423-9.

Kessler, D.J., 1981. Derivation of the collision probability between orbiting objects: the lifetimes of jupiter's outer moons. Icarus 48, 39–48. URL: http://linkinghub.elsevier.com/retrieve/pii/0019103581901512, doi:10.1016/0019-1035(81)90151-2.

King-Hele, D., 1987. Satellite orbits in an atmosphere: theory and application. Blackie, Glasgow and London.

Krisko, P.H., 2011. Proper Implementation of the 1998 NASA Breakup Model. Orbital Debris Quarterly News 15, 1–10.

Letizia, F., Colombo, C., Lewis, H.G., 2015a. Analytical model for the propagation of small debris objects clouds after fragmentations. Journal of Guidance, Control, and Dynamics 38, 1478–1491. doi:10.2514/1.G000695.

Letizia, F., Colombo, C., Lewis, H.G., 2015b. Collision probability due to space debris clouds through a continuum approach. Journal of Guidance, Control, and Dynamics URL: http://arc.aiaa.org/doi/abs/10.2514/1.G001382, doi:10.2514/1.G001382. accessed on September 10, 2015.

McInnes, C.R., 1993. An analytical model for the catastrophic production of orbital debris. ESA Journal 17, 293–305.

McInnes, C.R., 1994. Compact analytic solutions for a decaying, precessing circular orbit. The Aeronautical Journal 98, 357–360.

McInnes, C.R., 2000. Simple analytic model of the long term evolution of nanosatellite constellations. Journal of Guidance Control and Dynamics 23, 332–338. doi:10.2514/2.4527.

McKnight, D.S., 1990. A phased approach to collision hazard analysis. Advances in Space Research 10, 385–388. doi:10.1016/0273-1177(90)90374-9.

McKnight, D.S., Di Pentino, F.R., Knowles, S., 2014. Massive collisions in LEO – A catalyst to initiate ADR, in: 65th International Astronautical Congress, Toronto. IAC-14-A.6.2.1.

Nazarenko, A., 1997. The development of the statistical theory of a satellite ensemble motion and its application to space debris modeling, in: Second European Conference on Space Debris. URL: http://adsabs.harvard.edu/full/1997ESASP.393..233N.

Nazarenko, A., 2002. Modeling Technogenous Contamination of the Near-Earth Space. Solar System Research 36, 513–521. URL: http://link.springer.com/article/10.1023/A%3A1022113421686, doi:10.1023/A:1022113421686.

Portree, D.S.F., Loftus, J.P., 1999. Orbital Debris: A Chronology. Technical Report NASA/TP-1999-208856. NASA.

Rossi, A., Anselmo, L., Cordelli, A., Farinella, P., Pardini, C., 1998. Modelling the evolution of the space debris population. Planetary and Space Science 46, 1583–1596. doi:10.1016/S0032-0633(98)00070-1.

Smirnov, N., Nazarenko, A., Kiselev, A., 2001. Modelling of the space debris evolution based on continua mechanics, in: Third European Conference on Space Debris. URL: http://adsabs.harvard.edu/full/2001ESASP.473..391S.

Sykes, M., 1990. Zodiacal dust bands: Their relation to asteroid families. Icarus 9. URL: http://www.sciencedirect.com/science/article/pii/001910359090117R.

Valk, S., Lemaître, A., Deleflie, F., 2009. Semi-analytical theory of mean orbital motion for geosynchronous space debris under gravitational influence. Advances in Space Research 43, 1070–1082. doi:10.1016/j.asr.2008.12.015.

Vallado, D.A., 2013. Fundamentals of astrodynamics and applications. 4th ed., Springer. Pages 551–573, 619–688. ISBN: 978-1881883180.

White, A.E., Lewis, H.G., 2014. The many futures of active debris removal. Acta Astronautica 95, 189–197. doi:10.1016/j.actaastro.2013.11.009.

Xu, Y.L., Horstman, M., Krisko, P., Liou, J.C., Matney, M., Stansbery, E., Stokely, C., Whitlock, D., 2009. Modeling of LEO orbital debris populations for ORDEM2008. Advances in Space Research 43, 769 – 782. doi:`http://dx.doi.org/10.1016/j.asr.2008.11.023`.